Astronomy & Astrophysics

Coronal loop seismology using damping of standing kink oscillations by mode coupling

D. J. Pascoe, C. R. Goddard, G. Nisticò, S. Anfinogentov, and V. M. Nakariakov

Centre for Fusion, Space and Astrophysics, Department of Physics, University of Warwick, CV4 7AL, UK
e-mail: D.J.Pascoe@warwick.ac.uk

ABSTRACT

Context. Kink oscillations of solar coronal loops are frequently observed to be strongly damped. The damping can be explained by mode coupling on the condition that loops have a finite inhomogeneous layer between the higher density core and lower density background. The damping rate depends on the loop density contrast ratio and inhomogeneous layer width.

Aims. The theoretical description for mode coupling of kink waves has been extended to include the initial Gaussian damping regime in addition to the exponential asymptotic state. Observation of these damping regimes would provide information about the structuring of the coronal loop and so provide a seismological tool.

Methods. We consider three examples of standing kink oscillations observed by the Atmospheric Imaging Assembly (AIA) of the Solar Dynamics Observatory (SDO) for which the general damping profile (Gaussian and exponential regimes) can be fitted. Determining the Gaussian and exponential damping times allows us to perform seismological inversions for the loop density contrast ratio and the inhomogeneous layer width normalised to the loop radius. The layer width and loop minor radius are found separately by comparing the observed loop intensity profile with forward modelling based on our seismological results.

Results. The seismological method which allows the density contrast ratio and inhomogeneous layer width to be simultaneously determined from the kink mode damping profile has been applied to observational data for the first time. This allows the internal and external Alfvén speeds to be calculated, and estimates for the magnetic field strength can be dramatically improved using the given plasma density.

Conclusions. The kink mode damping rate can be used as a powerful diagnostic tool to determine the coronal loop density profile. This information can be used for further calculations such as the magnetic field strength or phase mixing rate.

Key words. magnetohydrodynamics (MHD) – Sun: atmosphere – Sun: corona – Sun: magnetic fields – Sun: oscillations – waves

1. Introduction

Coronal seismology as a method for determining fundamental plasma parameters is based on modelling magnetohydrodynamic (MHD) waves in the solar atmosphere and comparison of predicted behaviour with observations (see e.g. reviews by Andries et al. 2009; Stepanov et al. 2012; De Moortel & Nakariakov 2012; Pascoe 2014). One of the most common applications is the use of standing kink oscillations of coronal loops to infer the strength of the magnetic field (e.g. Nakariakov et al. 1999; Nakariakov & Ofman 2001; Van Doorsselaere et al. 2008b; White & Verwichte 2012). This method is based on the observation of transverse displacements of a loop as a function of time. Modelling this behaviour as a fast magnetoacoustic kink mode allows the observed period of oscillation and loop length to be related to the magnetic field strength and density profile. Verwichte et al. (2013) demonstrated that the results of such seismological inversions are consistent with values obtained by magnetic extrapolation and spectral observations. In addition to being a tool for remote plasma diagnostics, MHD waves might also have a significant role in the processes of coronal heating and solar wind acceleration (see e.g. reviews by Ofman 2010; Parnell & De Moortel 2012; Arregui 2015).

Observations of standing kink oscillations excited by flares or coronal mass ejections began in the late 1990s with the Transition Region And Coronal Explorer (TRACE; Aschwanden et al. 1999; Nakariakov et al. 1999). It was immediately evident that the oscillations were strongly damped, i.e. the oscillation would be observed for only a few cycles showing a steady decrease in amplitude. An understanding of the damping mechanism provides the opportunity for further seismological information by relating the observed damping time to plasma parameters. The strong damping of standing kink modes observed by TRACE was described by Ruderman & Roberts (2002) and Goossens et al. (2002) in terms of resonant absorption, i.e. the coupling of the observed transverse kink motions to localised (unobserved) azimuthal Alfvén waves.

Mode coupling or resonant absorption is a robust mechanism which occurs for coronal loops that have a finite inhomogeneous layer between their higher density (lower Alfvén speed) core and the lower density (higher Alfvén speed) background. The mechanism was first proposed by Sedláček (1971) and later discussed as a plasma heating mechanism by Chen & Hasegawa (1974) and Ionson (1978). Hollweg & Yang (1988) estimated that for coronal conditions the damping time would only be a few wave periods.

Ruderman & Roberts (2002) analysed the standing kink oscillation observed by Nakariakov et al. (1999) which was fitted with an exponential damping profile with a signal quality (ratio of decay time to period of oscillation) of $\tau_d/P \approx 3.4$. Resonant absorption theory relates the signal quality τ_d/P to the transverse density structure of the loop; the density contrast ratio (ρ_0/ρ_e) and the width of the inhomogeneous layer normalised to the loop radius (ϵ). The observed damping rate

therefore contains information about the loop structure. By making the assumption that the coronal loop has a density contrast ratio $\rho_0/\rho_e = 10$, Ruderman & Roberts (2002) calculated that $\epsilon = 0.23$ for the loop observed by Nakariakov et al. (1999). Similarly, Goossens et al. (2002) considered 11 oscillating loops and calculated values of $\epsilon = 0.16-0.49$, again under the assumption that each loop had a density contrast ratio of 10. Here we have ignored the slightly different definitions of loop radius used by Ruderman & Roberts (2002) and Goossens et al. (2002), which is discussed further by Van Doorsselaere et al. (2004). The definition used in this paper is the same as Goossens et al. (2002).

In the above examples, the need to assume a particular loop density contrast ratio is indicative of the general problem that the ratio of the damping rate to the period of oscillation τ_d/P is a single observable parameter that depends on two unknown parameters (ρ_0/ρ_e and ϵ). Seismological inversions based on this parameter therefore produce curves in parameter space; in other words, the inversion problem is ill-posed and has infinite solutions corresponding to different combinations of ρ_0/ρ_e and ϵ, though bounding values can be estimated (Arregui et al. 2007; Goossens et al. 2008). However, Pascoe et al. (2013) showed that damping of kink oscillations can occur in two different regimes, giving Gaussian and exponential damping profiles. Pascoe et al. (2013) proposed that a unique seismological inversion would be possible if a damping profile containing two characteristic times, corresponding to different damping rates expected at early and late times, could be fitted. In this paper, we apply this method to observational data from the Atmospheric Imaging Assembly (AIA) of the Solar Dynamics Observatory (SDO). Arregui et al. (2013) employed a version of the inversion technique using Bayesian analysis of the two fitted damping times to constrain the loop parameters and errors when the problem is well-posed, while Arregui & Asensio Ramos (2014) considered Bayesian analysis to derive structuring information even for the ill-posed case.

Tomczyk et al. (2007) discovered ubiquitous transverse velocity perturbations propagating in the corona. The oscillations have a broadband spectrum centred on a period of about 5 min. These have been interpreted as propagating kink waves (e.g. van Doorsselaere et al. 2008a) and, as with standing kink waves, are also found to be strongly damped in loop structures (Tomczyk & McIntosh 2009). Mode coupling was again used to account for this damping (e.g. Pascoe et al. 2010; Terradas et al. 2010). Numerical simulations of these strongly damped propagating kink waves by Pascoe et al. (2012) led to the discovery that the damping behaviour for early times is best described by a Gaussian profile rather than an exponential one. This was confirmed by an analytical treatment by Hood et al. (2013) which derived an integro-differential equation for the continuous variation of the amplitude for all times (see reviews by Pascoe 2014; De Moortel et al. 2016). Further analysis of the ubiquitous broadband propagating kink oscillations by Verth et al. (2010) accounted for the observed discrepancy between outward and inward propagating wave power and revealed evidence of a frequency-dependent damping rate, both consistent with mode coupling. However, the data were too noisy to distinguish between Gaussian or exponential profiles (Pascoe et al. 2015). Pascoe et al. (2016) recently reported examples of standing kink oscillations observed by SDO/AIA which appear to exhibit a Gaussian damping profile. The Gaussian regime is also evident in numerical studies of damped standing modes by Ruderman & Terradas (2013), and the subsequent phase mixing of the generated Alfvén waves by Soler & Terradas (2015).

Resonant absorption studies commonly employ a cylindrical geometry since this describes a range of common structures and provides the finite azimuthal wavenumber necessary for coupling. However, this symmetry is not a strict requirement. For example, Terradas et al. (2008) investigated the damping of standing oscillations for a 2D multi-stranded model, while Pascoe et al. (2011) simulated mode coupling of propagating wavepackets in asymmetric loops and multi-stranded inhomogeneous media. Similarly, in the context of magnetospheric oscillations, Russell & Wright (2010) studied resonant wave coupling in equilibria with a 2D structure perpendicular to the background magnetic field.

The analysis of the damping profile performed in this paper, and in Pascoe et al. (2016), is made possible by the high-resolution imaging data provided by SDO/AIA which allows detailed studies of kink oscillations (see also Aschwanden & Schrijver 2011; White & Verwichte 2012). High-resolution SDO data has also led to the discovery of low-amplitude decayless standing oscillations (Nisticò et al. 2013; Anfinogentov et al. 2013), which appear to be ubiquitous in active regions (Anfinogentov et al. 2015). The excitation mechanism for these low-amplitude oscillations is not yet understood, while a recent statistical study by Zimovets & Nakariakov (2015) demonstrates that the high-amplitude decaying kink oscillations are more commonly excited by low-coronal eruptions rather than blast waves launched by flares. The selectivity of the excitation is therefore connected with direct interaction with the erupting plasma, rather than interaction with an external wave (e.g. McLaughlin & Ofman 2008; Pascoe et al. 2009a; De Moortel & Pascoe 2009; Pascoe & De Moortel 2014).

Pascoe et al. (2016) found evidence of Gaussian damping regime for kink waves, and we extend that work in this paper to use observational damping profiles to provide seismological determinations of coronal loop parameters for the first time. In Sect. 2 we present our observations of damped standing kink modes using SDO/AIA. In Sect. 3 we describe the seismological inversion method for determining coronal loop parameters using the damping due to mode coupling. In Sect. 4 we use this seismological information to forward model the expected intensity profile for the loop, which is compared with the observational data to further constrain the loop parameters. Discussion and conclusions are presented in Sect. 5.

2. Observations by SDO/AIA

The kink oscillation events were selected from the catalogue compiled in Goddard et al. (2016) and also recently identified by Pascoe et al. (2016) as being suitable for investigating the kink mode damping profile. This selection was done on the basis of the loop being accurately identified and tracked for several consecutive cycles once the oscillation begins. They also have a period of oscillation that remains stable throughout the observation, and so we can reasonably assume these oscillations to be the result of a single excitation event and that the loop parameters (e.g. length and density contrast ratio) do not change significantly during the oscillation. We note, however, that not all of the events from Pascoe et al. (2016) are considered here owing to the greater requirement needed for our seismological method, which requires accurate fitting of two consecutive damping regimes (see Sect. 3).

As in Pascoe et al. (2016), the time–distance (TD) maps for the selected events were created using linear slits with a 5 pixel width perpendicular to the oscillating loop. SDO/AIA EUV 171 Å data is used, with a spatial resolution of 0.6 arcsec

Table 1. Selected SDO/AIA observations of standing kink modes used in the paper.

Loop No.	Catalogue event No.	Date	Time (UT)	L (Mm)
Loop #1	Event 43 Loop 4	2013 Jan. 7	06:38:11	222 ± 31
Loop #2	Event 31 Loop 1	2012 May 26	20:41:48	162 ± 31
Loop #3	Event 32 Loop 1	2012 May 30	08:58:00	234 ± 31
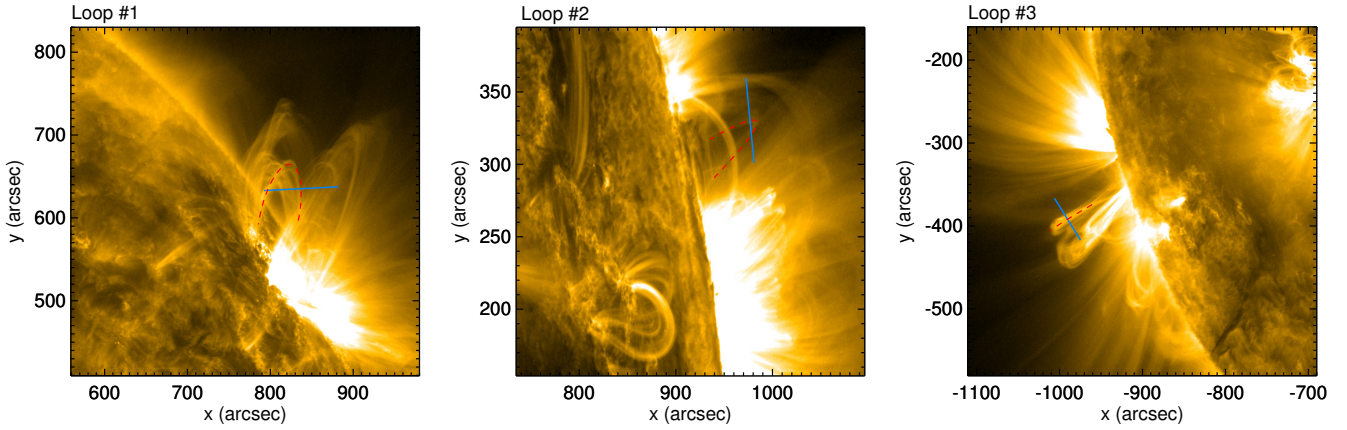
Fig. 1. SDO/AIA 171 Å images of the selected events. The oscillating loops are highlighted by the dashed red lines, which are either elliptical or linear fits depending on the loop orientation. The solid blue lines show the location of the particular slits chosen to create TD maps used for further analysis.

per pixel and temporal cadence of 12 s. A series of 100 such slits were created for each loop at different points along the axis and the slit that maximised the clarity of the TD map and the apparent amplitude of the oscillation was then chosen for further analysis. The chosen events are listed in Table 1, which shows the designation (loop number) used in this paper, the designation used in Goddard et al. (2016), the date and time of the event, and the estimated loop length L that will be used in Sect. 3. Figure 1 shows SDO images of the selected events.

3. Seismological inversion for damping due to mode coupling

Pascoe et al. (2013) produced a general spatial damping profile which describes the damping envelope of propagating kink waves for all times. It is based on the full analytical solution derived by Hood et al. (2013) and consists of two approximations combined together, a Gaussian profile for early times with damping length L_g and an exponential profile for later times with damping length L_d,

$$A(z) = \begin{cases} A_0 \exp\left(-\frac{z^2}{2L_g^2}\right) & z \leq h \\ A_h \exp\left(-\frac{z-h}{L_d}\right) & z > h \end{cases} \tag{1}$$

where $A_h = A(z = h)$ and the height at which the switch in profiles occurs is determined by the damping lengths

$$h = L_g^2 / L_d. \tag{2}$$

In this paper we consider standing kink modes which are instead characterised by considering a fixed point in space and measuring the variation of the oscillation amplitude in time. We can employ the same general damping profile using the change of variable $t = z/C_k$, which corresponds to the long wavelength limit for which the kink mode phase speed is the kink speed C_k. For a

standing mode with wavelength λ in a coronal loop of length L we have

$$C_k = \lambda/P \tag{3}$$

with $\lambda = 2L$ for the global or fundamental standing mode. The damping time and length scales are related to the coronal loop transverse density profile by

$$\frac{\tau_g}{P} = \frac{L_g}{\lambda} = \frac{2}{\pi \kappa \epsilon^{1/2}} \tag{4}$$

and

$$\frac{\tau_d}{P} = \frac{L_d}{\lambda} = \frac{4}{\pi^2 \epsilon \kappa}, \tag{5}$$

where $\epsilon = l/R$ is the normalised inhomogeneous layer width and $\kappa = (\rho_0 - \rho_e)/(\rho_0 + \rho_e)$ is a ratio of the internal density ρ_0 and the external density ρ_e. The constant of proportionality depends on the chosen density profile in the inhomogeneous layer. Here we use a profile that varies linearly from ρ_0 at $r \leq (R - l/2)$ to ρ_e at $r > (R + l/2)$, this being the only profile for which the full analytical solution is currently known. The constant of proportionality is known for the exponential component of the general damping profile for the case of other profiles (see discussions by e.g. Goossens et al. 2002; Roberts 2008).

The general damping profile for standing kink waves is thus given by
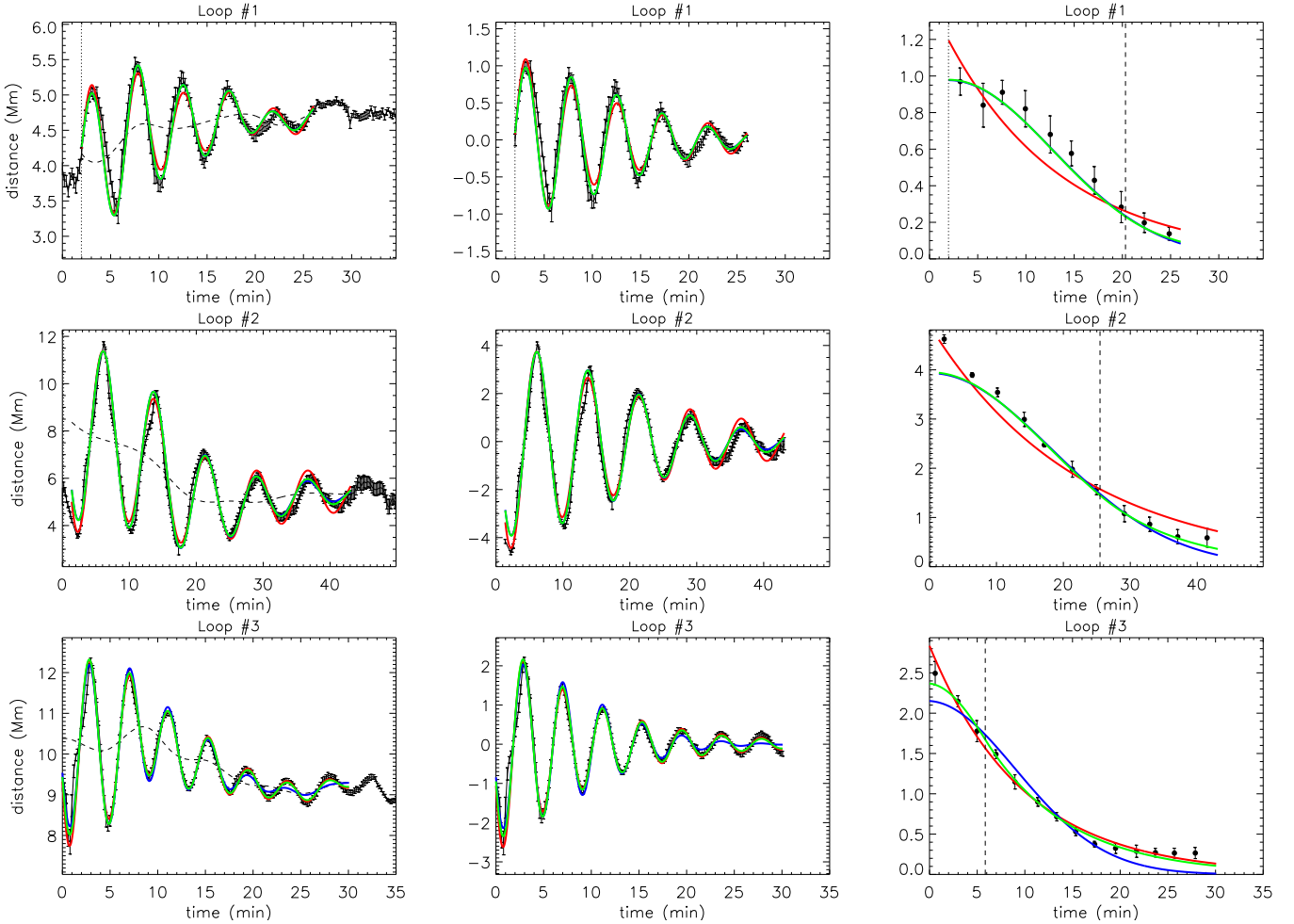
$$A(t) = \begin{cases} A_0 \exp\left(-\frac{t^2}{2\tau_g^2}\right) & t \leq t_s \\ A_s \exp\left(-\frac{t-t_s}{\tau_d}\right) & t > t_s \end{cases} \tag{6}$$

where $A_s = A(t = t_s)$ and the switch in profiles is at

$$t_s = h/C_k = \tau_g^2 / \tau_d. \tag{7}$$

The switch between Gaussian and exponential profiles is determined by the coronal loop density contrast ratio ρ_0/ρ_e as

$$N_c = \frac{t_s}{P} = \frac{h}{\lambda} = \frac{1}{\kappa} = \frac{\rho_0 + \rho_e}{\rho_0 - \rho_e} = \frac{\rho_0/\rho_e + 1}{\rho_0/\rho_e - 1} \tag{8}$$

Fig. 2. Kink oscillations fitted with a general damping profile. *Left panels*: locations of the loop axis as a function of time for the three loops we consider. The background trends are shown by the dashed lines and the detrended signals are shown in the *middle panels*. *Right panels*: absolute values of the detrended extrema with the damping envelopes. The best fit curves correspond to exponential (red), Gaussian (blue), and general damping (green) profiles. The vertical dotted and dashed lines denote the start time of the oscillation and the switch time t_s, respectively.

Table 2. Fitted parameters for kink oscillations as defined by Eqs. (6) and (9).

Loop No.	A_0 (Mm)	ϕ (rad)	P (min)	τ_g (min)	τ_d (min)	t_s (min)	c_0 (Mm)	c_1 (Mm/min)	c_2 (Mm/min^2)
Loop #1	0.98 ± 0.02	0.07 ± 0.03	4.73 ± 0.01	10.80 ± 0.27	6.35 ± 1.52	18.35 ± 4.29	3.89	0.083	-0.0022
Loop #2	-3.95 ± 0.02	-0.18 ± 0.01	7.65 ± 0.01	17.87 ± 0.15	12.63 ± 0.83	25.29 ± 1.62	9.14	-0.266	0.0043
Loop #3	-2.37 ± 0.03	-0.03 ± 0.01	4.17 ± 0.00	7.35 ± 0.24	8.81 ± 0.89	6.14 ± 0.48	10.53	-0.045	-0.0003

where N_c is the number of cycles of the oscillation after which the switch occurs. We therefore expect loops with larger density contrasts to transition from the Gaussian to the exponential profile sooner than loops with smaller density contrasts. This forms the basis of the seismological method for determining κ for an observed oscillation. The value of ϵ can then be calculated from the relation in Eqs. (4) or (5).

The displacement of the coronal loop axis by the kink oscillation is modelled as a damped sinusoid with a background trend. The background trend is typically assumed to be polynomial (e.g. Aschwanden 2009). As in Pascoe et al. (2016), we use spline interpolation to determine the background trends, which are shown as dashed lines in the left panels of Fig. 2. The detrended signals (middle panels of Fig. 2) are then fitted with a damped sinusoid of the form

$$A(t)\sin(\omega t - \phi). \tag{9}$$

The parameters A_0, $P = 2\pi/\omega$, ϕ, τ_g, τ_d, and t_s are determined by a Levenberg-Marquardt least-squares fit with data points weighted according to their errors. The fitted values are given in Table 2.

The background trend determined by spline interpolation allows the damped sinusoidal component of the oscillation to be identified as clearly as possible for accurate fitting of the damping profile. However, such trends cannot conveniently be numerically quantified and so in Table 2 we also give the parameters for a second-order polynomial trend of the form $c_0 + c_1 t + c_2 t^2$, which approximates the interpolated trend. This polynomial approximation is used in Sect. 4 to produce the forward modelled TD maps (see Fig. 6).

Figure 3 shows the seismological inversions for ρ_0/ρ_e and ϵ based on the kink mode damping profiles in Fig. 2. Using the exponential damping time τ_d alone produces a curve of possible
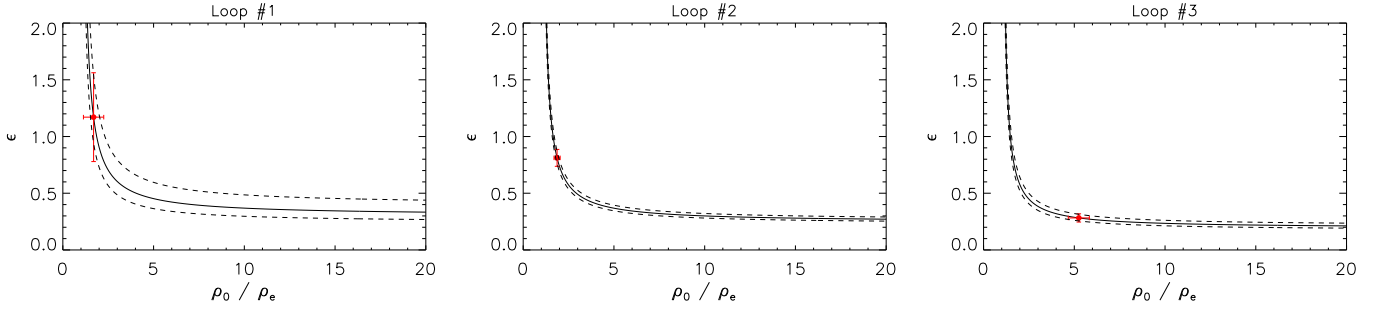
Fig. 3. Seismological inversions for the density contrast ratio and normalised layer width based on the kink mode damping profile. Using the exponential damping time τ_d alone produces a curve of possible values (error bars denoted by dashed lines). Using the general damping profile given by Eq. (6) determines ϵ and ρ_0/ρ_e simultaneously (red symbols with error bars).

Table 3. Seismologically determined loop parameters.

Loop No.	ρ_0/ρ_e	ϵ	R (Mm)	l (Mm)	C_k (Mm/s)	C_{A0} (Mm/s)	C_{Ae} (Mm/s)	B_0 (G)
Loop #1	1.69 ± 0.56	1.17 ± 0.39	1.54 ± 0.13	1.80 ± 0.62	1.56 ± 0.22	1.40 ± 0.30	1.82 ± 0.49	9.38 ± 2.56
Loop #2	1.87 ± 0.17	0.81 ± 0.07	2.59 ± 0.64	2.10 ± 0.56	0.71 ± 0.14	0.62 ± 0.12	0.85 ± 0.17	4.37 ± 0.88
Loop #3	5.25 ± 0.58	0.28 ± 0.04	3.34 ± 0.34	0.94 ± 0.15	1.87 ± 0.25	1.44 ± 0.21	3.30 ± 0.51	17.06 ± 2.63

values as discussed by Arregui et al. (2007) and Goossens et al. (2008), whereas using the general damping profile given by Eq. (6) produces unique seismological inversions (red symbols), i.e. single pairs of values for ρ_0/ρ_e and ϵ within a narrow range (error bars) associated with observational uncertainty, fitting accuracy, and the propagation of these errors through the calculations discussed below.

Our least-squares fit of the general damping profile returns the parameters (and error estimates) $P \pm \delta P$, $\tau_g \pm \delta\tau_g$, and $t_s \pm \delta t_s$. The seismological inversion is then calculated as

$$\tau_d = \tau_g^2 / t_s$$

$$\delta\tau_d = |\tau_d| \sqrt{4\left(\delta\tau_g/\tau_g\right)^2 + \left(\delta t_s/t_s\right)^2}$$

$$\kappa = P/t_s$$

$$\delta\kappa = |\kappa| \sqrt{\left(\delta P/P\right)^2 + \left(\delta t_s/t_s\right)^2}$$

$$\rho_0/\rho_e = (1 + \kappa) / (1 - \kappa)$$

$$\delta\left(\rho_0/\rho_e\right) = \rho_0/\rho_e \sqrt{2\left(\delta\kappa/\kappa\right)^2}$$

$$\epsilon = 4P/\left(\tau_d \pi^2 \kappa\right)$$

$$\delta\epsilon = |\epsilon| \sqrt{\left(\delta P/P\right)^2 + \left(\delta\tau_d/\tau_d\right)^2 + \left(\delta\kappa/\kappa\right)^2}. \quad (10)$$

We note that our fitting routine considers all three parameters t_s, τ_g, and τ_d simultaneously as given by Eq. (6), though only two of them are fitted independently and the third (here τ_d) given by Eq. (7). The values of ρ_0/ρ_e and ϵ are also given in Table 3. Additional loop parameters in Table 3 are determined as described below and in Sect. 4.

The observational estimate for the loop length $L \pm \delta L$ (Table 1) is used to calculate the kink speed using Eq. (3). In this paper we use the values given in Goddard et al. (2016). We can then determine the Alfvén speeds inside (C_{A0}) and outside (C_{Ae}) the coronal loop, subject to the approximation that the magnetic field strength is constant $B_0 = B_e$, consistent with the low β state of plasma in coronal active regions. This is possible since we have determined the density contrast independently by using the seismological inversion of the damping profile. However, the seismological determination of magnetic field strength still

requires the absolute value of the density to be known by some additional measurement or method. The calculations performed and associated errors are

$$C_k = 2L/P$$

$$\delta C_k = |C_k| \sqrt{\left(\delta L/L\right)^2 + \left(\delta P/P\right)^2}$$

$$C_{A0} = C_k / \sqrt{2/\left(1 + \rho_e/\rho_0\right)}$$

$$\delta C_{A0} = |C_{A0}| \sqrt{\left(\delta L/L\right)^2 + 2\left(\delta P/P\right)^2 + \left(\delta t_s/t_s\right)^2}$$

$$C_{Ae} = C_{A0} \sqrt{\rho_0/\rho_e}$$

$$\delta C_{Ae} = |C_{Ae}| \sqrt{\left(\delta L/L\right)^2 + 3\left(\delta P/P\right)^2 + 2\left(\delta t_s/t_s\right)^2}$$

$$B_0 = C_{A0} \sqrt{\mu_0 \bar\mu m_p n_0}$$

$$\delta B_0 = |B_0| \sqrt{\left(\delta L/L\right)^2 + 3\left(\delta P/P\right)^2 + 2\left(\delta t_s/t_s\right)^2}, \quad (11)$$

where $\mu_0 = 4\pi \times 10^{-7}$ H/m, $\bar\mu = 1.27$, $m_p = 1.6726 \times 10^{-27}$ kg, $n_0 = n_e\rho_0/\rho_e$, and here we assume a typical value of $n_e = 10^{15}$ m^{-3} (with no associated error). This estimate for n_e is the only parameter not determined from the observational data by the seismological method described in this paper. We note that the errors in the Alfvén speeds and B_0 can be written in terms of the error in the time of the switch between profiles t_s (as well as the usual δL and δP terms), since this time determines the density contrast ratio on which the kink speed depends. An additional term of $0.25\left(\delta n_0/n_0\right)^2$ is also required for δB_0 in the case of a measured n_0 with known error δn_0.

4. Forward modelling of time–distance maps

In Sect. 3 we considered the time-dependence of the oscillating loop and performed a seismological inversion to determine coronal loop parameters. In this section we use this information and the intensity profiles perpendicular to the loop axis to determine further loop parameters. In particular, we use the seismologically determined density contrast ratio and normalised inhomogeneous layer width $\epsilon = l/R$ to then calculate the inhomogeneous layer width l and loop radius R separately. This allows the
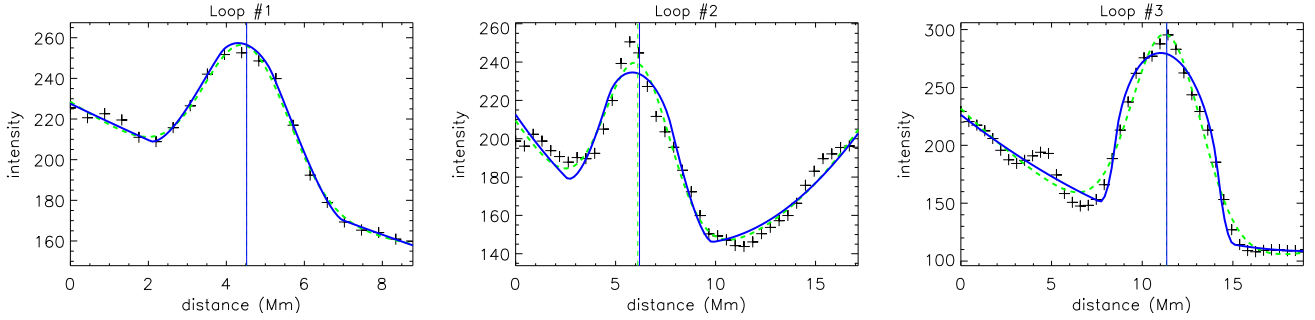
Fig. 4. Examples of fitting observational transverse intensity profiles with Gaussian (dashed green) and forward modelled (solid blue) fits. The vertical lines are the corresponding locations of the loop centre for each fitted profile.
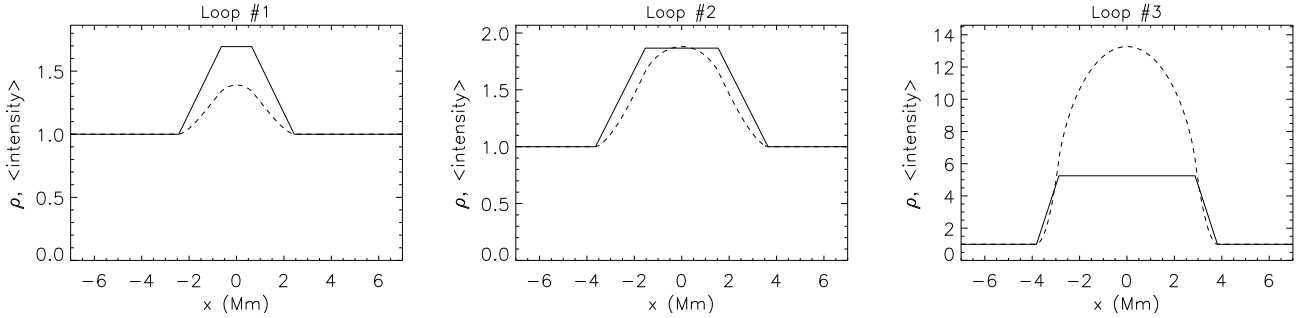
Fig. 5. Profiles for the seismologically determined transverse density (solid lines) and the corresponding averaged LOS intensity (dashed lines) for a cylindrical loop.

transverse loop density profile to be determined, and by combining this information with the time-dependence from Sect. 3 we create forward modelled TD maps.

Figure 4 shows examples for each loop of Gaussian (dashed green) and forward modelled (solid blue) fits to the observed transverse intensity profile. Each of these fits represents a single instance in time during the oscillation (which assumes that the loops do not perform unresolved, short-period oscillations during the SDO/AIA integration time). For each loop, approximately 100 such fits are used to calculate the mean value R (and standard deviation δR) given in Table 3. The corresponding density profiles (normalised to the external density) are given by the solid lines in Fig. 5.

The forward modelled intensity profile is calculated by assuming a cylindrically symmetric loop where the radial density profile is the same as that used in the mode coupling model, i.e. a linear variation in density from the internal to the external value across the inhomogeneous layer, and constant elsewhere (see Fig. 5). The intensity is then taken to be proportional to the square of the density and integrated along the line of sight (LOS), i.e. the loop is assumed to be optically transparent. Examples of the forward modelled intensity profile (averaged along the LOS) are shown by the dashed lines in Fig. 5. In comparison to the original density profile (solid lines) the intensity is smoother owing to the cylindrical symmetry. For example, the density is constant in the core region near the centre of the loop, whereas the corresponding intensity varies continuously since the thickness of the core region (and the entire loop) along the LOS is greatest at the centre of the loop. Similarly, near the outside edge of the inhomogeneous layer both the average loop density and the thickness of the loop along the LOS decrease with increasing distance from the loop centre.

Both the Gaussian and forward modelled intensity profiles in Fig. 4 also include a background term in the form of a second-order polynomial (in position). The vertical lines are the corresponding locations of the loop centre for each fitted profile.

The Gaussian and forward modelled profiles are both symmetric functions (although the background term may be asymmetric) and so give the same value for the location of the loop axis defined as the local maximum. The purpose of using the forward modelled profile is that the fit returns a value of loop radius R that has the same definition as the density profile used in the mode coupling model in Sect. 3 (and with ϵ constrained to the seismologically determined value). On the other hand, fitting a Gaussian profile to the intensity returns a width or standard deviation σ. We expect that $\sigma \sim R$, but with some unknown constant of proportionality of order unity (a comparison our fitting for R from the forward modelled profile with σ from the Gaussian fitting gives $\sigma/R \approx 0.6{-}0.7$ for our three loops). Additionally, there is no expression to determine l from σ, i.e. σ is a freely fitted parameter for the Gaussian fit, whereas for the forward modelled profile R is free but $\epsilon = l/R$ is known and fixed for the particular loop. From our fitting of the forward modelled density profiles to the observed intensity profiles we have $R \pm \delta R$. The seismologically determined ϵ from Eq. (10) then gives

$$
\begin{aligned}
l &= \epsilon R \\
\delta l &= |l| \sqrt{(\delta\epsilon/\epsilon)^2 + (\delta R/R)^2}.
\end{aligned} \tag{12}
$$

Figure 6 shows the observational (top panels) and forward modelled (bottom panels) TD maps. The forward modelled maps use the parameters given in Tables 2 and 3 (including the polynomial trend rather than the spline trend used in Sect. 3). The vertical dashed lines denote the start time of the oscillation. For convenience, the loop position is taken to be fixed before this time in the forward modelled TD maps. The symbols are the fitted locations of the loop centre for the observational data, as also shown in the left panels of Fig. 2. Since the forward modelling is based on the measured oscillation of a single loop, it only reproduces the intensity contribution from that loop, i.e. other structures or variations in the background intensity are not reproduced. The forward modelling also only considers the density dependence,
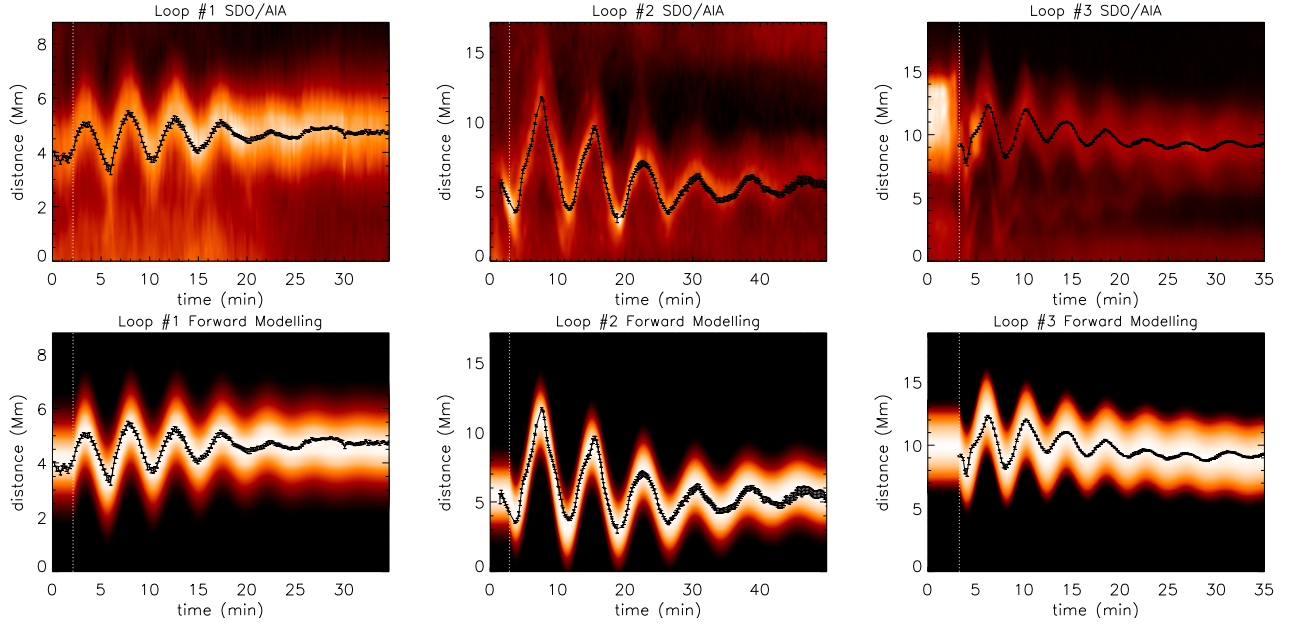
Fig. 6. Comparison of observational TD maps (*top*) with those produced by forward modelling (*bottom*) using the parameters given in Tables 2 and 3. The vertical dashed lines denote the start time of the oscillation. The symbols are the fitted locations of the loop centre for the observational data (see also Fig. 2).
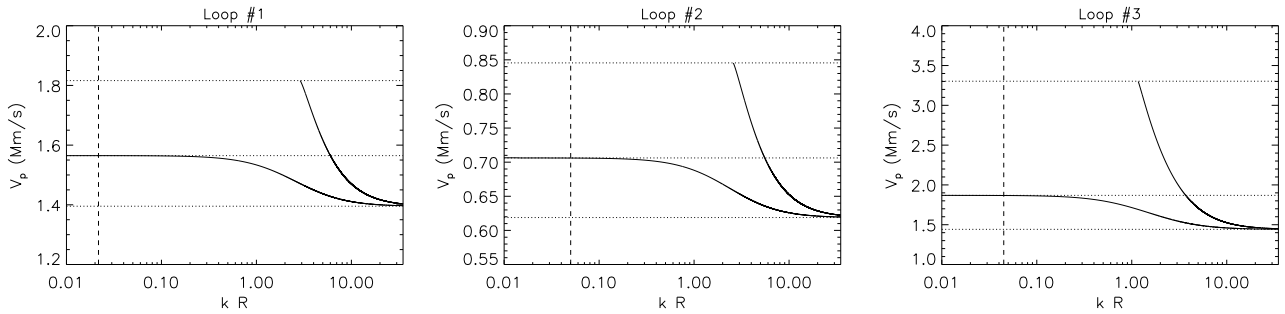
Fig. 7. Dispersion diagrams for the analysed loops showing the phase speed V_p of the kink and sausage modes as a function of the normalised wavenumber kR. The upper, middle, and lower dotted lines represent C_{Ae}, C_k, and C_{A0}, respectively. A logarithmic scale is used to emphasise the behaviour in the long wavelength limit $kR \ll 1$. The dashed lines correspond to the value for the global standing mode $kR = \pi R/L$.

and the density profile itself is taken as fixed during the oscillation. Variations in intensity due to variations in the density or temperature are therefore not considered. In the context of these features and limitations, the forward modelled TD maps demonstrate good agreement with the observational maps.

Next we briefly discuss two examples of further analysis of the observed coronal loops which are made possible by the information about the transverse loop structure revealed by the method in this paper.

4.1. Dispersion diagrams

Information about the Alfvén speed profile allows us to calculate the dispersion diagrams for the particular coronal loop. In Eq. (11) the kink speed is determined by the observed loop length and period of oscillation, which is based on the assumption that the oscillation phase speed V_p is the kink speed C_k. Using the seismologically determined loop density contrast ratio (and the assumption of a constant magnetic field) then gives the internal and external Alfvén speeds, which we use to calculate the dispersion diagrams. Using the loop radius found above then allows us to check the consistency of the long wavelength approximation used in our seismological method.

Figure 7 shows the dispersion diagrams for the three loops, i.e. the phase speed as a function of the wavenumber $k = 2\pi/\lambda$ normalised by the loop minor radius R. The upper, middle, and lower dotted lines represent C_{Ae}, C_k, and C_{A0}, respectively. A logarithmic scale is used to emphasise the behaviour in the long wavelength limit $kR \ll 1$ for which the kink mode phase speed tends to C_k. The other branch in each of the dispersion diagrams corresponds to the sausage mode for which the phase speed tends to C_{Ae} at some finite cut-off wavenumber $k_cR \sim 1$, beyond which the sausage mode experiences leakage from the loop. The dashed lines correspond to the value for the global standing mode $kR = \pi R/L$ and so in each case demonstrate that the long wavelength approximation $V_p \approx C_k$ is consistent. In each case we are also well within the leaky regime for sausage modes. Sausage modes do not experience mode coupling, but owing to leakage we would expect any excited sausage modes to have a low signal quality for loops with a small density contrast ratio (e.g. Cally 1986; Pascoe et al. 2007b; Vasheghani Farahani et al. 2014). On the other hand Nakariakov et al. (2012) show that the period depends on the transverse density profile in the long wavelength limit, which may provide additional seismological diagnostics.

The dispersion diagrams in Fig. 7 are calculated using the analytical solution for a magnetic cylinder given by

Edwin & Roberts (1983). This model does not include the finite inhomogeneous layer and so does not describe mode coupling at all, but here we only consider the dependence of the period of oscillation on the wavenumber. It is possible that the period of oscillation is itself modified by the presence of the inhomogeneous layer, in which case the seismologically determined density profile such as those given in Fig. 5 could be used to perform a numerical solution of the wave equation (e.g. Pascoe et al. 2007a), although it is beyond the scope of the present paper. Calculations by Van Doorsselaere et al. (2004) and Arregui et al. (2005) suggest that the effect of the finite inhomogeneous layer on the period of oscillation can be important for $\epsilon \gtrsim 1$, and so might be relevant for our loops 1 and 2. Yu et al. (2015) also show that the choice of density profile in the inhomogeneous layer has a small effect on the period of oscillation for standing kink modes in magnetic slabs. The diagrams also assume plasma $\beta = 0$, and we do not consider fluting modes or higher transverse harmonics of the sausage and kink modes.

4.2. Phase mixing and heating

The transfer of energy from collective transverse loop motions (kink waves) to localised azimuthal motions (Alfvén waves) by mode coupling is an ideal process. All the energy of the initial kink oscillation is eventually converted to Alfvén waves. In a uniform medium, Alfvén waves are very weakly dissipated. However, the mode coupling process we consider requires that the Alfvén waves be generated in a non-uniform medium, i.e. the inhomogeneous layer of the coronal loop. The continuous variation of the local Alfvén speed with position means the Alfvén waves will experience phase mixing which generates large transverse gradients in the waves (e.g. Heyvaerts & Priest 1983; Cally 1991; Hood et al. 2005; Soler & Terradas 2015). Equivalently, we can consider the characteristic spatial scale of the perturbations to be the phase mixing length L_{ph}, which continuously decreases over time. The seismological method presented in this paper gives information about the Alfvén speed profile transverse to the loop (see Fig. 5), which can be used to study the dissipation of the wave energy and consequent heating of the plasma. Here we present some simple estimates based on the assumption that the efficiency of the Alfvén wave dissipation mechanism is inversely proportional to the characteristic spatial scale of the wave, which is itself determined by phase mixing.

Phase mixing is a common phenomenon and has been studied in detail in several contexts. For Alfvén waves in the Earth's magnetospshere Mann et al. (1995) calculated the time dependence of the phase mixing length as

$$L_{ph} = \frac{2\pi}{\omega'_A t} \tag{13}$$

where $\omega'_A \approx k_\parallel v'_A$ and for our model with a linear profile in the inhomogeneous layer $v'_A = (C_{Ae} - C_{A0})/l$. This approximation was also found to accurately describe simulations of Alfvén waves generated by mode coupling of kink waves propagating along coronal loops by Pascoe et al. (2010).

Mann & Wright (1995) estimated the lifetime of poloidal Alfvén waves in the Earth's magnetosphere as $\tau_A = k_a/\omega'_A$, where k_a is the azimuthal wavenumber. For kink modes $k_a = 1/R$, and the Alfvén waves generated by mode coupling retain this ($m = 1$) symmetry. We can therefore rewrite τ_A in terms of the parameters used in this paper as

$$\tau_A = \frac{\epsilon L}{\pi (C_{Ae} - C_{A0})}. \tag{14}$$

The estimates of this phase mixing timescale for loops 1–3 are 197, 185, and 11 s, respectively. Evidently, the timescale is strongly dependent on the loop density contrast ratio which determines the change in Alfvén speed. While the Alfvén waves themselves cannot be resolved by modern instruments, these different phase mixing timescales may contribute to different heating rates for the loops. It may be possible to detect signatures of such variations in heating rates for different loops. The role of mode coupling in plasma heating has recently been studied by Okamoto et al. (2015) and Antolin et al. (2015) for transverse oscillations of prominences, in which the Kelvin-Helmholtz instability also generates small spatial scales in the inhomogeneous layer to allow efficient dissipation of the wave energy.

5. Discussion and conclusions

The full seismological method used in this paper is summarised below; we note the particular assumptions or approximations employed.

1. A TD map is produced for observational data such as SDO/AIA. The loop length is also estimated separately to calculate the kink mode wavelength and hence the kink speed C_k using Eq. (3).
2. The observational TD map is used to determine time series for the loop position, e.g. Gaussian fit of the transverse intensity profile to determine the position of the loop centre.
3. The detrended time series is fitted with a damped sinusoidal oscillation with the envelope being the general damping profile in Eq. (6). The density profile in the inhomogeneous layer is assumed to be linear (the only profile for which a full analytical solution is currently known).
4. The fitted general damping profile parameters are used for the seismological inversion to determine the loop density contrast ρ_0/ρ_e with Eq. (8), and the inhomogeneous layer width ϵ with Eqs. (4) or (5) (see also Eq. (10)).
5. The values of C_k and ρ_0/ρ_e can be used to determine the internal Alfvén speed C_{A0} as in Eq. (11). This uses the approximation of a constant magnetic field $B_0 = B_e$. The external Alfvén speed C_{Ae} can be determined similarly, and if the plasma density ρ_0 or ρ_e is known or can be estimated, the magnetic field strength B_0 can also be calculated.
6. The forward modelled intensity is calculated for the loop density profile using the seismological values of ρ_0/ρ_e and ϵ. Here we use the approximation that the temperature is constant and so the intensity is proportional to ρ^2 integrated along the LOS. The loop is also assumed to be cylindrical. Comparison of this model intensity profile to the observational intensity profile determines R by least-squares fitting, and hence l from Eq. (12).
7. Having obtained the Alfvén speed profile for the coronal loop, additional physical calculations can then be performed. For example, the dispersion diagrams (Sect. 4.1) or the phase mixing rate (Sect. 4.2).

The most important and novel component of this method in comparison with previous observational studies is the use of the general damping profile given by Eq. (6) to describe the decay of the kink oscillation due to mode coupling. Fitting this profile determines two damping timescales, τ_g for the Gaussian regime and τ_d for the exponential regime, and so provides us with an additional independent observable, making the problem well-posed and allowing a seismological inversion to be performed, which provides specific values for the density contrast ratio and normalised inhomogeneous layer width (within errors). Fitting only

the Gaussian or exponential component of the profile gives a single timescale and so the seismological inversion is a curve in parameter space, such as those shown in Fig. 3.

This method not only allows the loop density contrast ratio to be estimated, but also does so using a method which is independent of intensity or spectral measurements. The method requires that the effects of LOS integration in the corona permit the loop to be accurately tracked during its oscillation. However, if this is satisfied the subsequent estimates of ρ_0/ρ_e and ϵ are not affected by LOS integration effects (e.g. Cooper et al. 2003; De Moortel & Pascoe 2012; Viall & Klimchuk 2013).

The seismological determination of the magnetic field strength B_0 of coronal loops by observations of standing kink oscillations depends on four parameters; L, P, ρ_0/ρ_e, and ρ_0. The loop length and period of oscillation are determined directly from observational data, and the density contrast ratio is revealed by our method. However, some other method or observation is required for ρ_0 and so for this reason the magnetic field strengths given in Table 3 remain dependent on an assumed parameter. In any case the method we present is an improved technique for the description of the damping profile of the kink mode, and can be a powerful component of a larger seismological strategy which includes, for example, simultaneous observation of additional harmonics (e.g. Andries et al. 2005; Srivastava et al. 2013) or wave modes (e.g. Zhang et al. 2015), spatial seismology using time series from different locations (e.g. Verth et al. 2007; Pascoe et al. 2009b), temperature data from multiple bandpasses (e.g. Cheung et al. 2015), or information about the magnetic field from extrapolations (e.g. Verwichte et al. 2013) or numerical simulations (e.g. Chen & Peter 2015), in addition to any improvements to the theoretical modelling of the relevant physical processes.

References

Andries, J., Arregui, I., & Goossens, M. 2005, ApJ, 624, L57
Andries, J., van Doorsselaere, T., Roberts, B., et al. 2009, Space Sci. Rev., 149, 3
Anfinogentov, S., Nisticò, G., & Nakariakov, V. M. 2013, A&A, 560, A107
Anfinogentov, S. A., Nakariakov, V. M., & Nisticò, G. 2015, A&A, 583, A136
Antolin, P., Okamoto, T. J., De Pontieu, B., et al. 2015, ApJ, 809, 72
Arregui, I. 2015, Phil. Trans. Roy. Soc. London Ser. A, 373, 20140261
Arregui, I., & Asensio Ramos, A. 2014, A&A, 565, A78
Arregui, I., Van Doorsselaere, T., Andries, J., Goossens, M., & Kimpe, D. 2005, A&A, 441, 361
Arregui, I., Andries, J., Van Doorsselaere, T., Goossens, M., & Poedts, S. 2007, A&A, 463, 333
Arregui, I., Asensio Ramos, A., & Pascoe, D. J. 2013, ApJ, 769, L34
Aschwanden, M. J. 2009, Space Sci. Rev., 149, 31
Aschwanden, M. J., & Schrijver, C. J. 2011, ApJ, 736, 102
Aschwanden, M. J., Fletcher, L., Schrijver, C. J., & Alexander, D. 1999, ApJ, 520, 880
Cally, P. S. 1986, Sol. Phys., 103, 277
Cally, P. S. 1991, J. Plasma Phys., 45, 453
Chen, F., & Peter, H. 2015, A&A, 581, A137
Chen, L., & Hasegawa, A. 1974, Physics of Fluids, 17, 1399
Cheung, M. C. M., Boerner, P., Schrijver, C. J., et al. 2015, ApJ, 807, 143
Cooper, F. C., Nakariakov, V. M., & Tsiklauri, D. 2003, A&A, 397, 765
De Moortel, I., & Nakariakov, V. M. 2012, Roy. Soc. London Philos. Trans. Ser. A, 370, 3193
De Moortel, I., & Pascoe, D. J. 2009, ApJ, 699, L72

De Moortel, I., & Pascoe, D. J. 2012, ApJ, 746, 31
De Moortel, I., Pascoe, D. J., Wright, A. N., & Hood, A. W. 2016, Plasma Physics and Controlled Fusion, 58, 014001
Edwin, P. M., & Roberts, B. 1983, Sol. Phys., 88, 179
Goddard, C. R., Nisticò, G., Nakariakov, V. M., & Zimovets, I. V. 2016, A&A, 585, A137
Goossens, M., Andries, J., & Aschwanden, M. J. 2002, A&A, 394, L39
Goossens, M., Arregui, I., Ballester, J. L., & Wang, T. J. 2008, A&A, 484, 851
Heyvaerts, J., & Priest, E. R. 1983, A&A, 117, 220
Hollweg, J. V., & Yang, G. 1988, J. Geophys. Res., 93, 5423
Hood, A. W., Brooks, S. J., & Wright, A. N. 2005, Proc. Roy. Soc. London Ser. A, 461, 237
Hood, A. W., Ruderman, M., Pascoe, D. J., et al. 2013, A&A, 551, A39
Ionson, J. A. 1978, ApJ, 226, 650
Mann, I. R., & Wright, A. N. 1995, J. Geophys. Res., 100, 23677
Mann, I. R., Wright, A. N., & Cally, P. S. 1995, J. Geophys. Res., 100, 19441
McLaughlin, J. A., & Ofman, L. 2008, ApJ, 682, 1338
Nakariakov, V. M., & Ofman, L. 2001, A&A, 372, L53
Nakariakov, V. M., Ofman, L., Deluca, E. E., Roberts, B., & Davila, J. M. 1999, Science, 285, 862
Nakariakov, V. M., Hornsey, C., & Melnikov, V. F. 2012, ApJ, 761, 134
Nisticò, G., Nakariakov, V. M., & Verwichte, E. 2013, A&A, 552, A57
Ofman, L. 2010, Liv. Rev. Sol. Phys., 7
Okamoto, T. J., Antolin, P., De Pontieu, B., et al. 2015, ApJ, 809, 71
Parnell, C. E., & De Moortel, I. 2012, Roy. Soc. London Philos. Trans. Ser. A, 370, 3217
Pascoe, D. J. 2014, Res. Astron. Astrophys., 14, 805
Pascoe, D. J., & De Moortel, I. 2014, ApJ, 784, 101
Pascoe, D. J., Nakariakov, V. M., & Arber, T. D. 2007a, Sol. Phys., 246, 165
Pascoe, D. J., Nakariakov, V. M., & Arber, T. D. 2007b, A&A, 461, 1149
Pascoe, D. J., de Moortel, I., & McLaughlin, J. A. 2009a, A&A, 505, 319
Pascoe, D. J., Nakariakov, V. M., Arber, T. D., & Murawski, K. 2009b, A&A, 494, 1119
Pascoe, D. J., Wright, A. N., & De Moortel, I. 2010, ApJ, 711, 990
Pascoe, D. J., Wright, A. N., & De Moortel, I. 2011, ApJ, 731, 73
Pascoe, D. J., Hood, A. W., de Moortel, I., & Wright, A. N. 2012, A&A, 539, A37
Pascoe, D. J., Hood, A. W., De Moortel, I., & Wright, A. N. 2013, A&A, 551, A40
Pascoe, D. J., Wright, A. N., De Moortel, I., & Hood, A. W. 2015, A&A, 578, A99
Pascoe, D. J., Goddard, C. R., Nisticò, G., Anfinogentov, S., & Nakariakov, V. M. 2016, A&A, 585, L6
Roberts, B. 2008, in IAU Symp. 247, eds. R. Erdélyi, & C. A. Mendoza-Briceno, 3
Ruderman, M. S., & Roberts, B. 2002, ApJ, 577, 475
Ruderman, M. S., & Terradas, J. 2013, A&A, 555, A27
Russell, A. J. B., & Wright, A. N. 2010, A&A, 511, A17
Sedláček, Z. 1971, J. Plasma Phys., 5, 239
Soler, R., & Terradas, J. 2015, ApJ, 803, 43
Srivastava, A. K., Dwivedi, B. N., & Kumar, M. 2013, Ap&SS, 345, 25
Stepanov, A. V., Zaitsev, V. V., & Nakariakov, V. M. 2012, Stellar Coronal Seismology as a Diagnostic Tool for Flare Plasma (Wiley-VCH Verlag GmbH & Co. KGaA)
Terradas, J., Arregui, I., Oliver, R., et al. 2008, ApJ, 679, 1611
Terradas, J., Goossens, M., & Verth, G. 2010, A&A, 524, A23
Tomczyk, S., & McIntosh, S. W. 2009, ApJ, 697, 1384
Tomczyk, S., McIntosh, S. W., Keil, S. L., et al. 2007, Science, 317, 1192
Van Doorsselaere, T., Andries, J., Poedts, S., & Goossens, M. 2004, ApJ, 606, 1223
van Doorsselaere, T., Nakariakov, V. M., Verwichte, E., & Young, P. R. 2008a, in European Solar Physics Meeting 12, ed. H. Peter, 2.81
Van Doorsselaere, T., Nakariakov, V. M., Young, P. R., & Verwichte, E. 2008b, A&A, 487, L17
Vasheghani Farahani, S., Hornsey, C., Van Doorsselaere, T., & Goossens, M. 2014, ApJ, 781, 92
Verth, G., Terradas, J., & Goossens, M. 2010, ApJ, 718, L102
Verth, G., Van Doorsselaere, T., Erdélyi, R., & Goossens, M. 2007, A&A, 475, 341
Verwichte, E., Van Doorsselaere, T., Foullon, C., & White, R. S. 2013, ApJ, 767, 16
Viall, N. M., & Klimchuk, J. A. 2013, ApJ, 771, 115
White, R. S., & Verwichte, E. 2012, A&A, 537, A49
Yu, H., Li, B., Chen, S.-X., & Guo, M.-Z. 2015, ApJ, 814, 60
Zhang, Y., Zhang, J., Wang, J., & Nakariakov, V. M. 2015, A&A, 581, A78
Zimovets, I. V., & Nakariakov, V. M. 2015, A&A, 577, A4